$Q = 1$ for complete order, and 0 for total disorder). The equilibrium temperature-dependence of Q is given by the condition $\partial(\Delta G)/\partial Q = 0$. Fitting the data to this condition yields $a/h = 0.00523$, $b/h = 13.4$ and $T_c = 645$ K. The lower-temperature kinetically controlled Q–T–time(t) pathways are defined by the Ginzburg–Landau equation[14]:

$$\frac{dQ}{dt} = -\frac{\gamma \exp(-\Delta G^*/RT)}{2RT}\frac{\partial G}{\partial Q} \quad (2)$$

where γ is a frequency factor and ΔG^* is the activation energy for M1–M2 exchange. Substituting equation (1) into equation (2) and integrating we obtain:

$$t - t_0 = \int_{Q_0}^{Q} \frac{-2RT}{\gamma h \exp(-\Delta G^*/RT)\left(-1 + \frac{a}{h}(T - T_c)Q + \frac{b}{h}Q^3\right)} dQ \quad (3)$$

which we solve numerically to obtain the time-dependence of ordering behaviour away from equilibrium on both heating and cooling. The neutron data have been fitted to this solution, adopting the known T–t path of the experiment. The fit is shown in Fig. 1 by solid curves (non-equilibrium heating and cooling), and gives an activation energy of Mn–Fe exchange on M1 and M2 of 193 ± 3 kJ mol^{-1}. In doing so we have assumed $\log(\gamma h) = 13.1 \pm 0.5$, following the arguments of Harrison and Putnis in their analysis of cation ordering in spinel[15], as no calorimetric data exists for the enthalpy of ordering in olivine (from which one may compute h). Changing the activation energy changes the temperature at which the 'peak' of the $Q(T)$ curve occurs on heating.

Using these values, we can simulate ordering paths expected at any cooling rate. On rapid cooling, Q falls below the equilibrium path at some temperature T' and a low value is frozen-in down to low temperatures. Slower cooling generates higher values of 'quenched-in' Q at room temperature. We refer to this as the saturation value of Q, Q_{sat}, which increases with slower cooling rates. The M-site occupancies measured at room temperature thus reflect the cooling rate of a quench from temperatures above T'. This reiterates the conclusion that published quench experiments on olivine do not describe the equilibrium high-temperature partitioning behaviour, but instead simply reflect particular cooling of individual experiments. Furthermore, this indicates that the room-temperature structure of an olivine may be used as a geospeedometer for rapid cooling events, such as in volcanic rocks. The range of cooling rates is suggested by Fig. 2, which shows the expected Q–T paths of $(Fe_{0.5}Mn_{0.5})_2SiO_4$ olivine cooled at constant rates over 13 decades of dT/dt. Adopting this method we find that the initial value of Q of our $(Fe_{0.5}Mn_{0.5})_2SiO_4$ sample corresponds to a quench rate (from its initial synthesis conditions) of 1.5 ± 0.2 K s^{-1}, which agrees with our estimate of the average quench rate of the sample from the synthesis temperature. Equation (3) could equally easily be used to determine Q–T paths following Newton's law of cooling, or other more elaborate time–temperature paths such as the step cooling path of our neutron diffraction experiment.

By calculating the Q–T–t paths across a range of cooling rates, the relationship between dT/dt and Q_{sat} has been obtained (Fig. 3). We find a nonlinear relationship between Q_{sat} and $\log(dT/dt)$. The temperature corresponding to an equilibrium value of $Q = Q_{sat}$ is given on the right-hand ordinate. Our neutron experiments provided site occupancies with an error of less than 1%. Assuming that the same procedure can be carried out for Fe–Mg olivines crystallizing from picritic and basaltic liquids, and that site occupancies can be determined to 10%, this implies that at cooling rates slower than around 10^{-5} K s^{-1} the changes in cation partitioning would be less than the limits of precision, and hence it would be more difficult to resolve cooling rates slower than around 1 K per day. As well as being applied to deducing the eruption/cooling rates of volcanic rocks, we expect that it should be possible to obtain information on the cooling of high-crustal level, relatively thin, sheet-like bodies of thickness 10–15 m, and on the cooling of the outer parts of intrusions substantially larger than this, of the order of 50–100 m thick.

These results show that the cooling rate of an Fe–Mn olivine may be determined from its room-temperature structure alone, specifically from the M1–M2 site occupancies. We further illustrate this in Table 1, where we have used the reported room-temperature M1–M2 site occupancies of a number of natural and synthetic Fe–Mn olivines to determine their cooling rates. Non-convergent ordering in olivines clearly provides a viable new method for high-speed geospeedometry. We are pursuing this approach and its application in planned and current studies of Fe–Mg, Fe–Ni and Mg–Mn ordering in olivines. □

Received 5 December 1995; accepted 23 April 1996.

1. Virgo, D. & Hafner, S. S. *Earth planet. Sci. Lett.* **14,** 305–312 (1972).
2. Princivalle, F. *Miner. Petrol.* **43,** 121–129 (1990).
3. Ottonello, G., Princivalle, F. & Della Giusta, A. *Phys. Chem. Miner.* **17,** 301–312 (1990).
4. Artioli, G., Rinaldi, R., Wilson, C. C. & Zanazzi, P. F. *Am. Miner.* **80,** 197–200 (1995).
5. Henderson, C. M. B., Knight, K. S., Redfern, S. A. T. & Wood, B. J. *Science* **271,** 1713–1715 (1996).
6. Seifert, F. A. & Virgo, D. *Science* **188,** 1107–1109 (1975).
7. Ganguly, J. & Tazzoli, V. *Am. Miner.* **79,** 930–937 (1994) .
8. Kroll, H., Schlenz, H. & Phillips, M. W. *Phys. Chem. Miner.* **21,** 555–560 (1994).
9. Kroll, H. & Knitter, R. *Am. Miner.* **76,** 928–941 (1991).
10. Huppert, H. E. & Sparks, R. S. J. *Earth planet. Sci. Lett.* **92,** 397–405 (1989).
11. Gibb, F. G. F. & Henderson, C. M. B. *Contr. Miner. Petrol.* **109,** 538–545 (1992).
12. Marsh, B. D. *J. Petrol.* **30,** 479–530 (1989).
13. Carpenter, M. A., Powell, R. & Salje, E. K. H. *Am. Miner.* **79,** 1053–1067 (1994).
14. Carpenter, M. A. & Salje, E. K. H. *Mineralog. Mag.* **53,** 483–504 (1989).
15. Harrison, R. J. & Putnis, A. *Am. Miner.* (in the press).
16. Shinno, I. *J. Jap. Ass. Miner. Petrol. econ. Geol.* **75,** 343–352 (1980).
17. Annersten, H., Adetunji, J. & Filippidis, A. *Am. Miner.* **69,** 1110–1115 (1984).
18. Brown, G. E. Jr *Rev. Miner.* **5,** 275–381 (1982).

ACKNOWLEDGEMENTS. This work was supported by Rutherford Appleton Laboratory.

Constraints from seismic anisotropy on the nature of the lowermost mantle

J.-M. Kendall* & P. G. Silver†

* Department of Earth Sciences, University of Leeds, Leeds LS2 9JT, UK
† Department of Terrestrial Magnetism, Carnegie Institute of Washington, 5241 Broad Branch Rd, NW, Washington DC 20015, USA

The D″ layer lies at the bottom of the Earth's rocky mantle, and separates it from the liquid metal-alloy core. This region, extending from the core–mantle boundary to a few hundred kilometres above (Fig. 1), is geodynamically analogous to the more easily studied lithosphere, at the top of the mantle. The structure of D″ may reflect the style of lower-mantle convection, the nature of core–mantle interaction and perhaps even the fate of subducting lithosphere[1]. Observations of lithospheric seismic anisotropy have provided valuable insight into the nature of the upper-mantle boundary layer, but discussion of lower-mantle seismic anisotropy has been somewhat contentious[2–5]. Here we present evidence, from seismic waves that have traversed the lowermost mantle beneath the Caribbean region, for a zone of seismic anisotropy below the D″ discontinuity, which in this region lies 250 km above the core–mantle boundary. The anisotropy is most probably due to horizontal layering or aligned inclusions of a material with differing shear-wave velocity. If D″ is a graveyard for subducted lithosphere, a plausible explanation of the anisotropy may be the contrast between cold lithospheric mantle and material that formerly constituted the oceanic crust, which may have lower shear-wave velocity owing to the presence of melt.

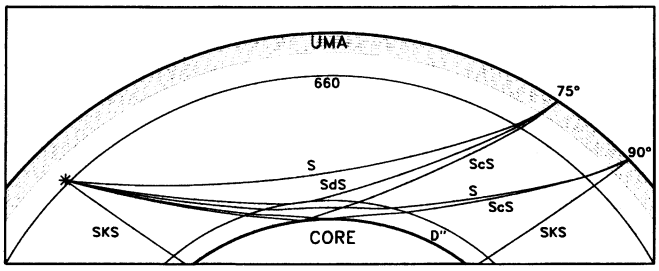

FIG. 1 A sketch of the seismic S-wave phases analysed at epicentral distances 75° and 90°. The 660-km discontinuity separates the upper and lower mantle; UMA refers to the region of upper-mantle anisotropy. Like those analysed in this study, the earthquake (indicated by an asterisk) is near the bottom of the upper mantle. In our study area a seismic discontinuity lies atop the D″ region 250 km above the core–mantle boundary[14].

Seismic tomography has shown that the largest lateral variations in lower-mantle velocities are at the base of the mantle[6,7]. Similarly, studies of core-diffracted phases have shown strong velocity variations within D″ (ref. 8). Lay and Helmberger[9] presented the first definitive evidence for a D″ discontinuity 250–300 km above the core–mantle boundary (CMB); later analyses of P- and S-wave data have revealed that the discontinuity exhibits strong lateral variations and is not a global feature[9–13]. It has also been proposed that D″ may be anisotropic[2–4]. Observations of anomalous high-amplitude diffracted SV phases (shear waves polarized in the source–receiver plane and diffracted along the CMB) have been attributed to D″ anisotropy, but these observations have been somewhat inconclusive as they can be explained with relatively simple isotropic structures[5]. Here we present strong evidence for D″ anisotropy in a region below Central America and the Caribbean (Fig. 2). Unlike previous studies, our analysis uses broad-band data and concentrates on travel times for S-wave arrivals which are primarily pre-diffracted. Our data set is unique in that we have sufficient coverage to analyse phases which turn above and within the D″ region thereby allowing us to constrain the anisotropy to the D″ region.

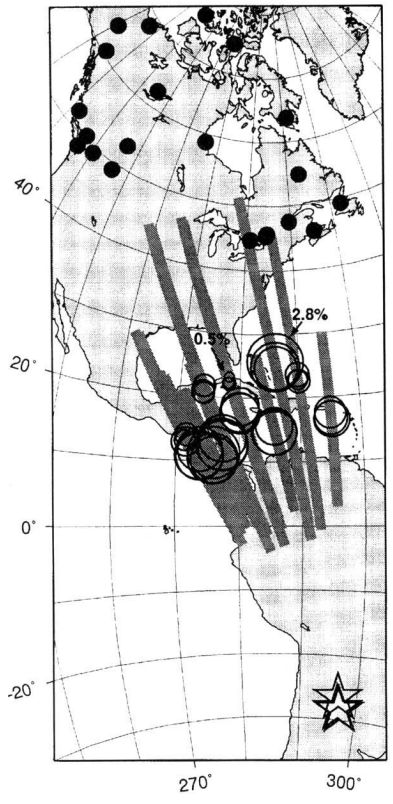

FIG. 2 A Cassini equal-area projection of the region of study. Filled circles show the stations of the Canadian National Seismograph Network (CNSN), and the stars show the epicentres of the three earthquakes studied. The range of epicentral distances spanned by the network is 70° to 110°. The interpreted S-wave anisotropy is plotted at the surface projection of source/station midpoints and the size of the circle is proportional to the degree of anisotropy (the extreme cases are marked). The extent of the sampled D″ region is indicated by a grey swath for each event–station raypath which enters D″

The broad-band data are from South American earthquakes recorded on the recently refurbished Canadian National Seismograph Network (CNSN; Fig. 2). Horizontally polarized, shear-wave (SH) data that image this region show clear evidence of a precursor to the core-reflected phase ScS. This has been interpreted as a reflection from a discontinuity 250 km above the CMB with a velocity contrast of 2.75% across the interface[9,14]. Here we compare the SH signals with the SV signals, looking for evidence of shear-wave splitting that is diagnostic of seismic anisotropy[15]. The phases we consider are primarily pre-diffracted phases, S and ScS, although five stations record diffracted arrivals, S_{diff}.

The earthquakes considered are very deep (>575 km) thus mitigating effects due to source-side upper-mantle anisotropy. The effects of receiver-side upper-mantle anisotropy cannot be dismissed so easily. Waveforms from many Canadian stations exhibit significant amounts of SKS splitting indicating receiver-side upper-mantle anisotropy[15,16]. It is therefore imperative that interpretations of lower-mantle anisotropy must first account for the upper-mantle anisotropy. To do this, we take independent estimates of upper-mantle anisotropy from observations of SKS splitting from events with a wide range of azimuths[15,17]. Measurements of upper-mantle anisotropy have been published for some of the CNSN stations[16] and we have made our own measurements for those stations without published values. Because the SKS measurements are from a variety of azimuths, the observed splitting must be due to anisotropy where ray paths are most similar which, for this case, is the upper mantle. Furthermore, the significant variation in splitting magnitude and orientation between receivers suggests that the anisotropy is confined to the upper mantle[15].

We localize the source of lower-mantle anisotropy to the D″ region through the analysis of phases that turn above and below the D″ discontinuity Figure 1 shows the phases under consideration: at 75°, S turns above the D″ region, SdS reflects off the D″ discontinuity. (250 km above the CMB in this area) and ScS reflects off the CMB. The splitting measured on S-arrivals that turn in the lower mantle above the D″ region can be entirely explained by anisotropy in the upper mantle as they show good agreement with independent SKS-splitting measurements. It is difficult to measure ScS splitting at these distances (<80°) owing to interference from SKS and SKKS, but the few reliable estimates that we can make show significantly more splitting. In such cases the magnitude and orientation of the ScS splitting is significantly different from that measured for SKS from a range of azimuths at the same station.

Beyond 80° the S and ScS arrivals are only separated by a few seconds in travel time, and are thus hard to isolate in a seismogram. Furthermore, standard splitting analysis is difficult as the radial and transverse component waveforms are quite different (Fig. 3). Instead we simply measure δt from the separation in travel-time onset after making a correction for upper-mantle anisotropy. Whereas the separation in SH and SV travel times for rays which turn above D″ can be explained by upper-mantle anisotropy, those for rays which turn within D″ show greater values of δt thereby constraining most of the lower-mantle anisotropy to the D″ region. The S-ScS and S_{diff} data show large delay

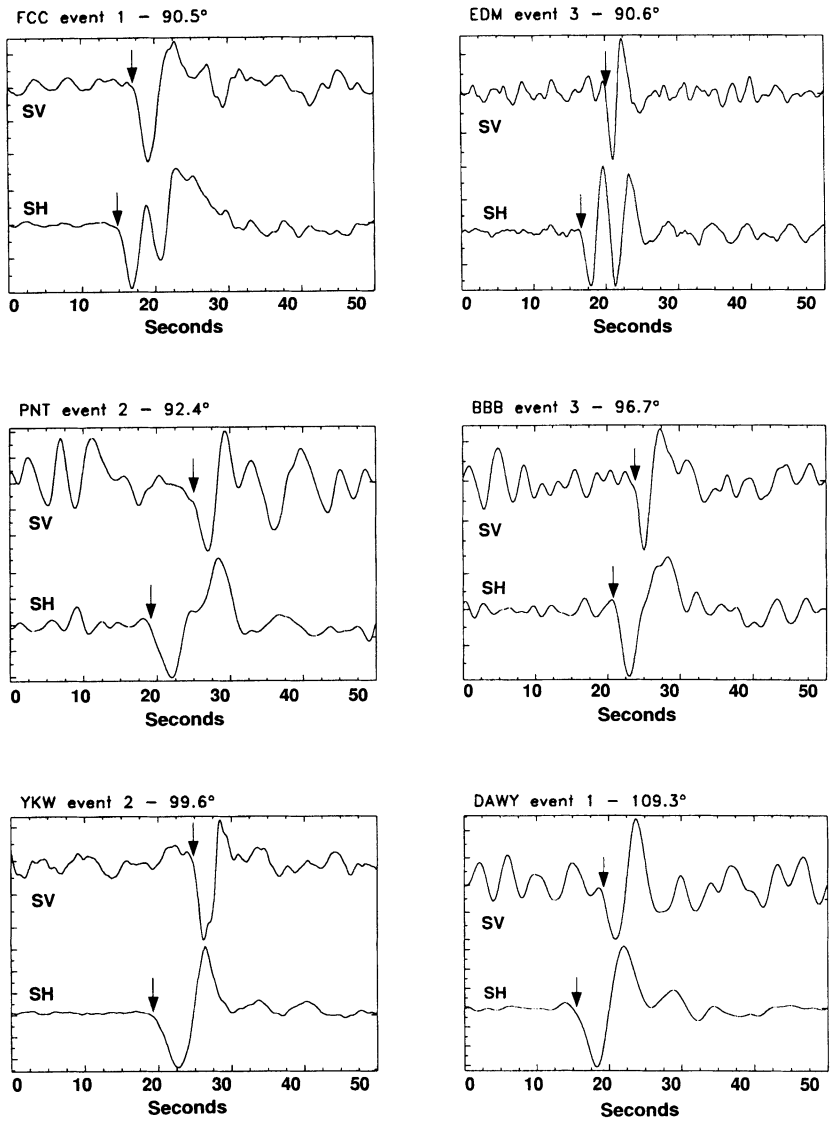

FIG. 3 Travel-time separations between arrivals on the radial (upper) and transverse (lower) components at stations beyond 90°. These seismograms (velocity records) have been corrected for upper-mantle anisotropy and represent ~15% of the data analysed; they were selected to show the splitting most clearly. The nearer stations record S and ScS arrivals which are only a few seconds apart, while the more distant station, DAWY, records the core diffracted phase, S_{diff}. Despite differences in waveform character, it is very clear that there are dramatic differences in the onset of the radial and transverse arrivals with the SH component always leading the SV component.

times (3–9 seconds) with the SH component always leading the SV component (Fig. 3).

The delay time depends both on the intrinsic anisotropy and horizontal extent of the anisotropy, which is in turn also dependent on the assumed thickness of the anisotropic region. As a conservative estimate, we assume that the anisotropic region extends from the CMB to the discontinuity 250 km above the CMB[14] and that the anisotropy is uniformly distributed along the entire path through a D″ model (SKNA1[14]) for this region. The results suggest 0.5–2.8% anisotropy along corridors 1,000–2,800 km in length, with an average values of 1.8% (Fig. 2). Signals that arrive at roughly 90° sample only the upper few tens of kilometres of D″ and yet they still exhibit significant shear-wave splitting. This implies that the anisotropy is vertically distributed throughout most of the D″ region. The variability in the estimated anistropy may be due to variability in the thickness of the D″ layer throughout this region.[14]

Three important pieces of evidence strongly suggest that D″ beneath the Caribbean is transversely isotropic. First, in our study area the SH phase is always faster than the SV phase. Second, rays with near-vertical paths through D″ (such as SKS) show no sign of splitting from this depth range[18]. This is consistent with transverse isotropy, but not with azimuthal anisotropy. The final argument comes form waveform modelling. The observed waveforms agree well with synthetic reflectivity waveforms for isotropic models with a discontinuity 250 km above the CMB, except that there is a large travel-time separation between the radial and transverse component seismograms that the isotropic models cannot explain. Such simplicity in the waveforms strongly suggests transverse isotropy because the SH and SV systems are decoupled for this case[19].

Any model for D″ must satisfy the observed symmetry and magnitude of the anisotropy, and the discontinuous increase in SH-wave velocity (v_{SH}) at the top of D″ in this region[14]. It appears unlikely that the anisotropy is due to the lattice preferred orientation (LPO) of lower-mantle minerals. Recent experiments suggest that perovskite, probably the most abundant mineral in the lower mantle, fails to develop strain-induced LPO[18]. It is also difficult to satisfy the seismic constraints with the alignment of other lower-mantle minerals with significant single crystal anisotropy (for example, cubic MgO and tetragonal stishovite). It is more probable that the anisotropy within D″ is due to the horizontal alignment of inclusions (within a matrix) or near-horizontal layering of materials with differing isotropic shear velocities[20]. Both models give rise to long-wavelength transverse isotropy with a vertical symmetry axis and exhibit $v_{SH} > v_{SV}$ (where v_{SV} is the SV wave velocity) for horizontally propagating waves[21–23]. These models are thus consistent with the form of the observed anisotropy.

We model the anisotropy using a theory for aligned spheroidal inclusions[22,23] (Fig. 4). The magnitude of anisotropy depends

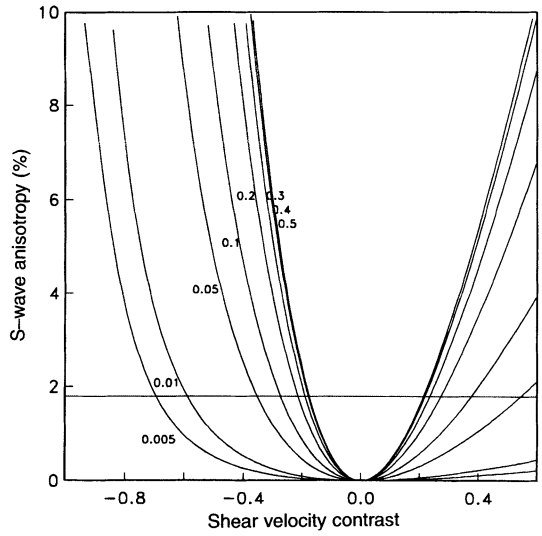

FIG. 4 Modelling the per cent anisotropy due to the preferential alignment of horizontal penny-shaped inclusions using the theory of Tandon and Weng[22] and Sayers[23]. The matrix velocity is 7.5 km s^{-1} and the inclusions have an aspect ratio of 0.01. The different curves are the per cent anisotropy as a function of velocity contrast for different inclusion volume-fractions (given on the curves). The shear-velocity contrast is defined as $(v_2 - v_1)/v_1$, where v_2 is the velocity of the inclusion material and v_1 is the velocity of the matrix. The average observed anisotropy (1.8%) is marked for reference (horizontal line). As the S-wave velocity of the inclusions tends to zero, very small inclusion volume-fractions can explain the observed anisotropy. Numerical experiments show little variation in S-wave anisotropy as the inclusion aspect-ratio gets smaller (eventually the medium can be effectively treated as being layered). Cigar-shaped inclusions (aspect ratio >1.0) require much higher volume fractions to explain the observed anisotropy.

primarily on the volume fraction of the inclusions, the inclusion aspect ratio and the shear velocity contrast. The aspect ratio of the inclusions can vary from that of cigar-shapes to that of penny-shapes, but it is much easier, in terms of orientation and volume fraction, to satisfy the observations with penny-shaped inclusions. As the inclusions get very flat (aspect ratio <0.001) there is good agreement with the results for alternating layers[21].

One simple model that is not consistent with the data has the matrix velocity equal to that of the zone just above D″, and the inclusion velocity faster. This requires unrealistic inclusion velocities (in excess of 10 km s^{-1}) and predicts too large a velocity discontinuity. This leads to the significant conclusion that both components have elastic properties distinct from the mantle just above D″. One important class of models that is efficient in producing anisotropy is characterized by inclusions of partial melt, as its shear velocity is nearly zero. The potential existence of melt in the lower mantle is uncertain, as is the geometry and alignment of such melt inclusions. There is little consensus on the geometry of melt inclusions in even lithospheric rocks[24], but melt inclusions with aspect ratios of the order of 0.05 have been observed in peridotites[25]. Less than 1% melt can explain the observed anisotropy if we assume that the melt exists in thin ellipsoidal disks (for aspect ratios <0.05) that are aligned owing to higher shear stresses. In such small quantities this produces less than a 1% reduction in v_{SH} and, consequently, the matrix must be about 3–4% fast.

We consider two possible mechanisms for producing a layered D″ region with the appropriate seismological properties. The first is the 'reaction-zone' hypothesis[26,27], where D″ is thought to contain silicate and iron-alloy products of a reaction between the mantle and core. As iron alloys have shear velocities 30–40% lower than silicates[27], this model could account for the anisotropy, if a 5% iron-alloy concentration (Fig. 4) segregated into horizontally elongated inclusions, throughout the 250 km thickness of D″. The introduction of Fe into D″, however, will have a general tendency to reduce shear velocities. In particular, taking the chemical reaction proposed by Knittle and Jeanloz[26], the aggregate v_{SH} of the reaction products is lowered by up to 6% (depending on the amount of Fe reacting), compared to the starting perovskite material.

The second mechanism is motivated by the increasingly compelling seismological observations that slabs descend into the lower mantle[28–30]. In such a scenario, the folded slabs may lie horizontally on the CMB[20,31,32]. The differing seismic properties of the former-harzburgite and former-basalt components of the slab could give rise to the anisotropy, while the high v_{SH} for D″ could be achieved through the retained thermal anomaly of the slab. Assuming that the basalt fraction is 0.1, then the contrast has to be at least 20% (Fig. 4). If there is a low-melting-temperature component within former-basalt, resulting from the relatively high concentrations of Fe, Al and Ca, a fraction of the former-basalt could have a significantly reduced shear modulus. A simple model is that melt within the basalt lowers its overall seismic velocity, and that the anisotropy results from the layering of the slower basalt and fast lithosphere. Recent melting experiments on probable basaltic components indeed suggest significant lowering (by ~2,000 K) of the melting point of perovskite due to Al and Ca[33]. If true, then 'old slabs' would provide an explanation for the overall properties of this region. Furthermore, lower-mantle tomography shows evidence for a vertical, slab-like feature extending down to the CMB (the so-called Caribbean anomaly), which has been attributed to the subduction of the former Farallon plate[30,34]. The hypothesis of a slab graveyard at the CMB is in principle straightforward to test and if true, would suggest that slabs play a major role in the mantle's two major thermal boundary layers, at the surface and CMB. □

Received 24 January; accepted 23 April 1996.

1. Loper, D. E. & Lay, T. *J. geophys. Res.* **100,** 6397–6420 (1995).
2. Vinnik, L., Farra, V. & Romanowicz, B. *Geophys. Res. Lett.* **16,** 519–522 (1989).
3. Vinnik, L., Romanowicz, B., LeStunff, Y. & Makeyeva, L. *Geophys. Res. Lett.* **22,** 1657–1660 (1995).
4. Lay, T. & Young, C. J. *Geophys. Res. Lett.* **18,** 1373–1376 (1991).
5. Maupin, V. *Phys. Earth Planet. Inter.* **87,** 1–32, (1995).
6. Masters, T. G., Bolton, H. F. & Shearer, P. M. *Eos* (abstr.) **73,** 201 (1992).
7. Su, W.-J., Woodward, R. L. & Dziewonski, A. M. *J. geophys. Res.* **99,** 16429–16454 (1994).
8. Wysession, M. E., Okal, E. A. & Bina, C. R. *J. geophys. Res.* **97,** 8749–8764 (1992).
9. Lay, T. & Helmberger, D. V. *Geophys. J. R. astr. Soc.* **75,** 799–837 (1983).
10. Weber, M. & Davis, J. P. *Geophys. J. Int.* **102,** 231–255 (1990).
11. Garnero, E. J., Helmberger, D. V. & Grand, S. P. *Phys. Earth planet. Inter.* **79,** 335–347 (1993).
12. Kendall, J.-M. & Shearer, P. M. *J. geophys. Res.* **99,** 11575–11590 (1994).
13. Nataf, H.-C. & Houard, S. *Geophys. Res. Lett.* **20,** 2371–2374 (1993).
14. Kendall, J.-M. & Nangini, C. *Geophys. Res. Lett.* **23,** 399–401 (1996).
15. Silver, P. G. & Chan, W. W. *Nature* **335,** 34–39 (1988).
16. Bostock, M. G. & Cassidy, J. F. *Geophys. Res. Lett.* **22,** 5–8 (1995).
17. Vinnik, L. P., Kind, R., Kosarev, G. L. & Makeyeva, L. I. *Geophys. J. Int.* **99,** 549–559 (1989).
18. Meade, C. P., Silver, G. & Kaneshima, S. *Geophys. Res. Lett.* **22,** 1293–1296 (1995).
19. Doornbos, D. J., Spiliopoulos, S. & Stacey, F. D. *Phys. Earth planet. Inter.* **41,** 225–239 (1986).
20. Weber, M. *Geophys. Res. Lett.* **23,** 2531–2534 (1994).
21. Backus, G. E. *J. geophys. Res.* **67,** 4427–4440 (1962).
22. Tandon, G. P. & Weng, G. J. *Polymer Composites* **5,** 327–333 (1984).
23. Sayers, C. *Int. J. Solids Structures* **29,** 2933–2944 (1992).
24. Schmeling, H. *Phys. Earth planet. Inter.* **41,** 34–57 (1985).
25. Faul, U. H., Toomey, D. R. & Waff, H. S. *Geophys. Res. Lett.* **21,** 29–32 (1994).
26. Knittle, E. & Jeanloz, R. *Science* **251,** 1438–1443 (1991).
27. Jeanloz, R. *A. Rev. Earth planet. Sci.* **18,** 357–386 (1990).
28. Creager, K. C. & Jordan, T. H. *J. geophys. Res.* **91,** 3573–3589 (1986).
29. Van der Hilst, R., Engdahl, R. & Spakman, W. *Geophys. J. Int.* **105,** 264–302 (1993).
30. Grand, S. P. *J. geophys. Res.* **99,** 11591–11621 (1994).
31. Silver, P. G., Carlson, R. W. & Olson, P. *A. Rev. Earth planet. Sci.* **16,** 477–541 (1988).
32. Christensen, U. R. & Hofmann, A. W. *J. geophys. Res.* **99,** 19867–19884 (1994).
33. Shen, G. & Lazor, P. *J. geophys. Res.* **100,** 17699–17713 (1995).
34. Engebretson, D. C., Kelley, K. P., Cashman, H. J. & Richards, M. A. *GSA Today* **2,** 93–100 (1992).

ACKNOWLEDGEMENTS. We thank P. Shearer and J. Vidale for constructive reviews, and M. H. Weber, V. Maupin, G. Helffrich, C. Sayers, J. Ritsema, S. van der Lee, C. Bina, R. Hemley and D. Mao for further helpful comments. We commend the seismology group at the Geological Survey of Canada for the installation and operation of the CNSN, and the distribution of the resulting high-quality data.